COMPARISON OF CELL- AND VERTEX CENTERED DISCRETIZATION METHODS FOR FLOW IN A TWO-DIMENSIONAL DISCRETE FRACTURE-MATRIX SYSTEM

H. HÆGLAND, A. ASSTEERAWATT, H. K. DAHLE, G. T. EIGESTAD, AND R. HELMIG

Abstract. Simulations of flow for a discrete fracture model in fractured porous rocks have gradually become more practical, as a consequence of increased computer power and improved simulation and characterization techniques. Discrete fracture models can be formulated in a lower-dimensional framework, where the fractures are modeled in a lower dimension than the matrix, or in an equi-dimensional form, where the fractures and the matrix have the same dimension.

When the velocity of the flow field is needed explicitly, as in streamline simulation of advective transport, only the equi-dimensional approach can be used directly. The velocity field for the lower-dimensional model can then be recovered by post-processing which involves expansion of the lower-dimensional fractures to equi-dimensional ones.

In this paper, we propose a technique for expanding lower-dimensional fractures and we compare two different discretization methods for the pressure equation; one vertex-centered approach which can be implemented as either a lower- or an equi-dimensional method, and a cell-centered method using the equi-dimensional formulation. The methods are compared with respect to accuracy, convergence, condition number, and computer efficiency.

1. Introduction

Fractured formations occur commonly in nature. Folding, faulting, and subsidence of sediments over geologic time cause fracturing. The more brittle the rock, the more intensely it fractures. Fractures can range in size from microns to hundreds of kilometers, and the accurate modeling of flow through such systems is important for many types of problems, including the management of water and energy resources and CO_2-sequestration [14, 15, 27].

Mathematical models based on continuum theory for quantifying flow and transport through fractured rocks can be classified into 1) continuum models, or 2) discrete fracture models, or 3) hybrid models, see e.g. [11, 14, 27, 51, 55, 60]. The models differ in their representation of the heterogeneity of the fractured media, and whether they are formulated in a deterministic or a stochastic framework.

In this paper we consider a discrete fracture model for flow in fracture-matrix system in two space dimensions (2D). Discrete fracture models [4, 23, 27, 60] allow quantification of many flow and transport phenomena that

Date: February 6, 2009.

Key words and phrases. Streamline tracing, Time-of-flight, Irregular grids.

are not adequately captured by single- or multi-continuum models. An advantage of the discrete fracture approach is that it can account explicitly for the effects of individual fractures on fluid flow and transport.

However, the contrast in permeability between fractures and the porous matrix may span many orders of magnitude and can vary highly in space [27], which is a major difficulty in modeling fluid flow in fractured rock [23]. Furthermore, due to the complex geometry of the model, unstructured grids are required for the discretization of the domain. Also, the heterogeneous and anisotropic behavior of the permeability is challenging for the numerical modeling of the system, and proper averaging of permeability between the computational cells is crucial [29].

Transport models are used for understanding and predicting the geological system using tools like break-through curves, arrival time and storage behavior. The outcome of transport simulations strongly depends on the distribution of velocities in the fractures [23]. The velocity distribution cannot, in general, be determined analytically, and must be obtained numerically from the solution of a flow (pressure) equation. Hence, desirable properties of a numerical scheme for flow simulation include: a) efficient approximation and solution of the flow (pressure) equation, b) local mass conservation, and c) high-accuracy approximation of the velocity field. The importance of efficiency is further increased by the need for considering Monte Carlo simulations.

Two approaches exist for discrete fracture models. If the matrix is (almost) impermeable and only interconnected fractures contribute to the flow, discrete fracture network models are appropriate [4, 23]. In this work we will consider a discrete-fracture-matrix (DFM) model [27]. This approach apply when both fractures and matrix play a significant role for the flow and transport processes and the model can not be homogenized. Two model approaches exist for the DFM model: In the DFM lower-dimensional formulation (DFML) [41, 44, 45, 49, 58], fractures are modeled as line segments in 2D, and as planar regions in 3D, whereas in the DFM equi-dimensional formulation (DFME) [13, 19, 46, 57, 58, 66], fractures are modeled in the same dimension as the matrix. The DFML has been more common than the DFME, since modeling fractures as lower-dimensional objects simplifies grid generation and data requirements. However, when the velocity of the flow field is needed explicitly, as in streamline simulation of advective transport [24], only the equi-dimensional approach can be used directly. The velocity field for the lower-dimensional model must be recovered by a post-processing step which involves an expansion of the lower-dimensional fractures to equi-dimensional ones [38].

In this paper, we consider a discrete fracture model where fractures are modeled as lower dimensional objects [58] in a geostatistical fracture generator [8]. The domain is assumed to be in 2D, such that fractures are modeled as line segments. A technique for expanding lower-dimensional fractures is proposed, and we investigate different discretization methods for flow on both DFML grids and DFME grids. Extensions to 3D is briefly discussed

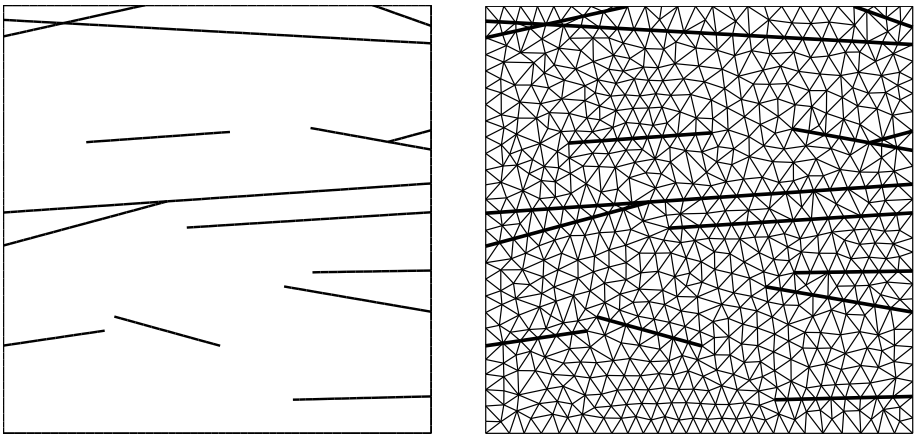

FIGURE 1. Left: A realization from the geostatistical fracture generator FRAC3D [62]. The fractures in black are modeled as lower dimensional objects, i.e. line segments. Right: Discretization of the realization in the left figure using the mesh generator ART [34]. Note that some estimate of fracture width (or aperture) must be provided by the fracture generator.

in the next section. A vertex-centered box scheme is compared with a cell-centered multi-point flux approximation. Section 3 introduces the vertex-centered and cell-centered finite volume methods. Section 4 compares the methods numerically for several test cases of increasing complexity. To illustrate that the fracture expansion also facilitate tracing of streamlines, we provide streamline calculations which demonstrate the convergence of the numerical velocity field. Finally, Section 5 concludes the paper.

2. Expansion of fractures

We consider fractures modeled as lower dimensional objects [58] by a geostatistical fracture generator [8]. A sample 2D realization is shown in Figure 1 (left). When fractures in a lower-dimensional model are subsequently expanded to have the same dimension as the matrix, we obtain a so-called equi-dimensional fracture model.

The fractures may be expanded before, or after the discretization of the fracture field. Usually the fractures will be very thin compared to the size of the domain. If a relative coarse mesh is being used around the fractures, e.g., as in Figure 1 (right), the size of the mesh elements will be much larger than the fracture aperture. In this case the fracture must be expanded *after* the grid generation. For a very fine mesh, however, the size of the triangles may be similar to the fracture aperture, or smaller. In this case, the fractures should be expanded *before* the grid is generated.

We will henceforth only consider cases where the fractures are expanded after the triangulation. We also assume that a constant aperture can be associated with each fracture segment, using a parallel plate model for the

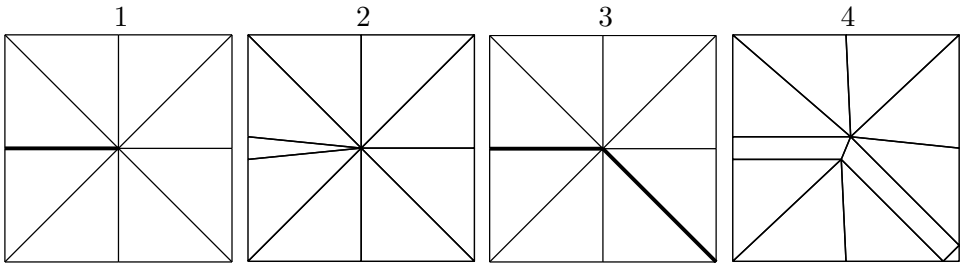

FIGURE 2. The cases $\varrho = 1$ and $\varrho = 2$. Sub figure 1) and 2): A single fracture ending. Sub figure 3) and 4): Two fractures meeting

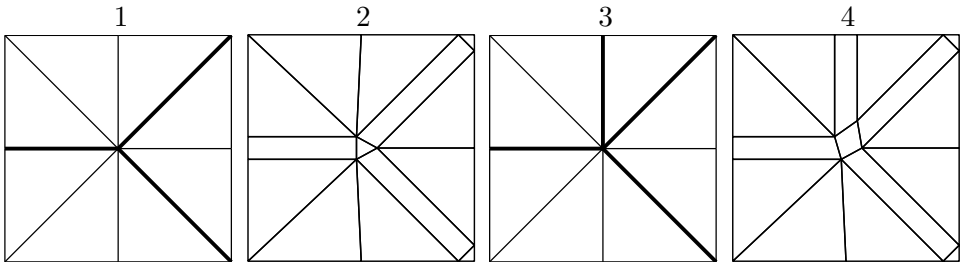

FIGURE 3. The cases $\varrho = 3$ and $\varrho = 4$. Sub figure 1) and 2): Three fractures meeting. Sub figure 3) and 4): Four fractures meeting

fractures [12]. The fractured domain is in 2D and will be discretized with triangles, such that the fractures coincides with the triangle edges. To simplify the presentation, we will assume that all fractures have the same aperture.

2.1. **Interior points.** The expansion algorithm is based on the number ϱ of fractures meeting at a vertex. We consider the cases of ϱ equal to 1, 2, 3, 4, and 5. Higher degrees are treated similar to degree 5. The reason for considering case 3, 4 and 5 separately, is related to the type of acceptable elements in the grid: triangles and quadrilaterals are permitted and can be used for the central element when $\varrho = 3$ and $\varrho = 4$, respectively. For $\varrho \geq 5$, the central element must be split into sub triangles, as shown later.

The case $\varrho = 1$, corresponds to a single fracture ending at an interior vertex, see Figure 2. A single fracture can be expanded in variety of ways, see e.g. [35, 53, 52, 54, 59]. This topic will not be investigated further in this work, here we use a single triangle as shown in Figure 2 (Left). The case $\varrho = 2$ is handled using two trapezoidal elements, see Figure 2 (Right). The case $\varrho = 3$, is shown in Figure 3 (Left). If the permeability of the three fractures is the same, this case can be handled using three trapezoids and a central triangle. If the permeability of the three fractures is different, the permeability of the central triangle can be calculated using a generalized harmonic mean [45], or the central triangle can be split into three sub triangles, each of which correspond to one of the fracture edges. The case $\varrho = 4$ is shown in Figure 3 (Right). In this case four trapezoids and a central quadrilateral are used, if the permeability of the fractures is different, the central quadrilateral may be split into four sub triangles. The

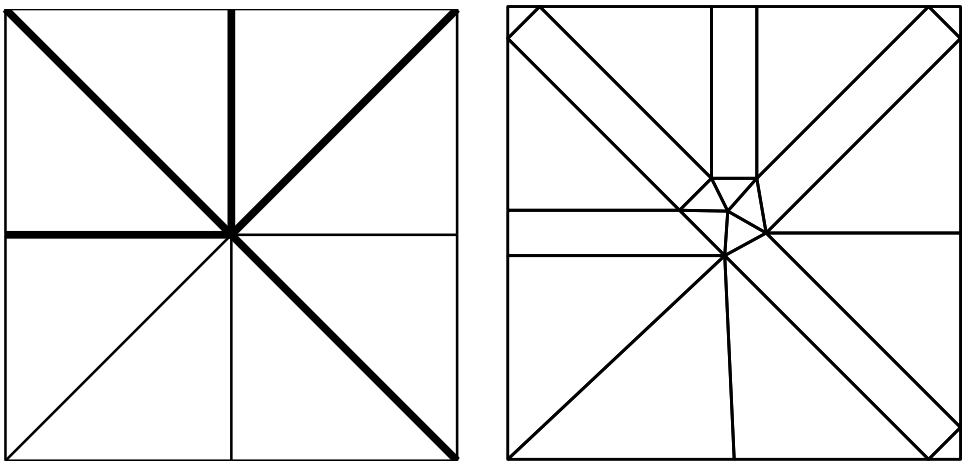

FIGURE 4. Five fractures meeting

case $\varrho = 5$ is shown in Figure 4. Cases of $\varrho > 5$ are handled in a similar fashion.

2.2. **Boundary points.** Boundary vertices with ending fractures are handled similar to interior vertices. If the boundary is flat at the vertex and only a single fracture is ending at the vertex, see e.g. the vertical fracture in Figure 4 (Right), then no extra element at the boundary is needed. If the boundary is not flat, or two or more fractures are meeting at the vertex, extra elements, either triangles or quadrilaterals are inserted at the boundary vertex, see also Figure 4 (Right).

2.3. **Extension to 3D.** Obviously, the expansion procedure in 3D is more complicated than for the 2D case. In the lower-dimensional form, each fracture will be modelled as a plane. A single plane not crossing any other planes, can then be expanded with hexahedral elements. Two planes will cross each other along a line if they are not parallel. The intersection line can also be expanded with hexahderal elements. Three non-parallel planes (with normal vectors not lying in the same plane) cross each other along three lines and in a single point, see [68]. The crossing point would be discretized with a hexahedral element. Four planes will cross each other along six lines and in three points. The points corresponds to intersections of the three possible groups of three planes taken from a group of four planes. It is highly unlikely that four planes cross in a single point. More than 4 planes will cross along lines and in points corresponding to groups of 3 planes.

3. Finite volume methods for elliptic problems

The flow equation for a single phase flowing in a porous medium is given by

$$-\nabla \cdot \boldsymbol{K} \nabla P = f, \tag{1}$$

for a permeability tensor $\boldsymbol{K}$, pressure P, and a source term f.

For general anisotropic and inhomogeneous medium, the permeability tensor is represented by a space-dependent full tensor. Layered and fractured

media involving large discontinuities in the permeability require numerical schemes with a continuous flux and a proper definition of transmissibility across cell-edges. Furthermore, the discrete features of the media and the general geometry of the media require the use of general unstructured grids. Since a simple two-point flux approximation is only applicable for the special case of a $\boldsymbol{K}$-orthogonal grid [2], more robust methods must be considered in our context.

Many schemes that preserve flux continuity on general unstructured grids have been developed, like mixed-finite element methods [16, 7, 6, 5], discontinuous Galerkin methods [20], mimetic finite difference methods [43, 61] and control-volume mixed finite element methods [17].

In this paper, we focus on two different finite volume methods (FVMs) [33] applicable to the discrete fracture model. The idea of a FVM is to discretize the domain into a mesh of finite volumes (or control volumes). Then the divergence form of the equation is exploited by integrating over a finite volume and using Gauss' theorem to convert the result into surface integrals which are discretized [50].

The most common FVM schemes are either cell-centered (block-centered), in which the primal grid cells are used to define the control volumes, or vertex-centered (point-distributed), in which control volumes are constructed around the primal grid vertices.

3.1. **The box method.** The box methods [48] are vertex-centered FVMs that can be formulated as a finite element method. Generally, a finite element method involves two spaces, the test- and the trial-space. The box method can be cast in the finite element setting with a trial space of piecewise polynomials over the primary grid, and a test space over the dual grid [48]. Since the trial functions will be different from the test functions, the box scheme can be treated as a Petrov-Galerkin finite element method [21].

For the box-scheme considered herein, the test functions are piecewise constant, and the trial functions are conforming piecewise linear polynomials. This kind of box scheme has also been called control-volume finite element method [9], finite volume element method [18], generalized difference method [48], and subdomain collocation method [42, 69].

Consider first the case of no fractures. The domain is discretized with triangular and/or quadrilateral elements E_j, $j = 1, \ldots, N^e$, and vertices $\boldsymbol{\mathcal{V}}_i$, $i = 1, \ldots, N^v$, where N_e is the total number of elements in the grids, and N_v is the total number of vertices in the grid. In the box method, one algebraic equation corresponds to every vertex in the primary mesh. The boxes are usually constructed as a dual mesh of an underlying grid. There are various ways to introduce the dual mesh, e.g., the Voronoi mesh based on the circumcenter [18, 48], or the Donald-mesh, based on the barycenter [10, 21, 32].

For the Donal-mesh the secondary dual mesh is defined by connecting the barycenter (centroid) of each element E_j with edge midpoints. The dual mesh divides each element into three or four sub quadrilaterals depending on the type of element (triangle/quadrilateral). The union of all sub quadrilaterals adjacent adjacent to a vertex $\boldsymbol{\mathcal{V}}_i$ is denoted Ω_i^B, or the control volume associated with $\boldsymbol{\mathcal{V}}_i$, see Figure 5 (left).

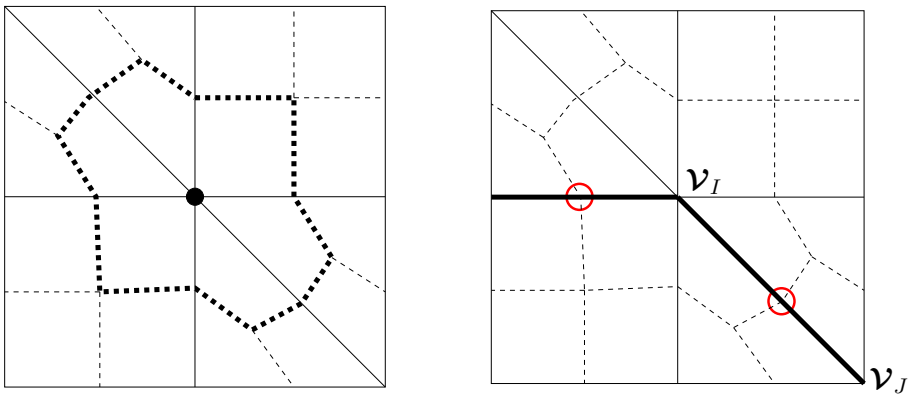

FIGURE 5. Left: Sample grid with no fractures consisting of a primary grid of two quadrilaterals and four triangles. The dual grid is indicated by dashed lines. The control volume associated with the central vertex (black circle) is indicated by the heavy dashed line. Right: Grid with fractures; intersection points indicated with red circles. A fracture intersects the dual mesh at its midpoint. The vertices $\boldsymbol{\mathcal{V}}_I$ and $\boldsymbol{\mathcal{V}}_J$ are the end points of a fracture.

As for the finite element method, the unknown in Equation (1), $P = P(x, y)$ is approximated using basis functions ϕ_i, $i = 1, \ldots, N^v$, weighted by discrete values $\hat{P}_i \equiv P(\boldsymbol{\mathcal{V}}_i)$, i.e., $P \approx \tilde{P} = \sum \phi_i \hat{P}_i$. A basis function is a piecewise continuous function such that its restriction to a triangular element will be a linear function, whereas its restriction to a quadrilateral is an isoparametric mapping of a bilinear function on a reference element [22, 64]. As usual, the basis functions ϕ_i are local functions, meaning that they are identically zero outside Ω_i^B.

The approximation of P with $\tilde{P}$ now leads to a residual in Equation (1), $\nabla \cdot \tilde{\boldsymbol{q}} - \nabla \cdot \boldsymbol{q} = \nabla \cdot \tilde{\boldsymbol{q}} - f$, where $\tilde{\boldsymbol{q}} = -\boldsymbol{K} \nabla \tilde{P}$. In the method of weighted residual [69], the weighted integral of the residual over the whole domain is set to zero,

$$\int_\Omega W_i (\nabla \cdot \tilde{\boldsymbol{q}} - f) dV = 0, \qquad i = 1, \ldots, N^v, \tag{2}$$

for each weight function W_i, $i = 1, \ldots, N^v$. The Box-method uses the simple form,

$$W_i(x) = \begin{cases} 1 & x \in \Omega_i^B \\ 0 & x \notin \Omega_i^B. \end{cases} \tag{3}$$

The application of the divergence theorem to (2) now leads to a set of N^v surface integrals over the boundaries of each control volume Ω_i^B. For triangular elements, these integrals can be evaluated analytically, whereas for quadrilateral elements the gradient of the pressure is not constant on each element, and numerical integration is required. In the numerical experiments in this paper we used a midpoint rule to evaluate the fluxes for quadrilateral elements.

Assuming an element-wise constant permeability, the N_v integrals can be expressed as

$$\sum_{j=1}^{N_{t,i}} \sum_{k=1}^{3} \gamma_{i,j,k} \hat{P}_{i,j,k} = f_i \qquad i = 1, \ldots, N^v. \tag{4}$$

Here, we have assumed a grid of only triangular elements, and the sum on k is running over the three vertices of each triangle j contributing to the control volume Ω_i^B. There are $N_{t,i}$ triangles contributing to Ω_i^B, and $\hat{P}_{i,j,k}$ refers to the pressure at local corner number k of triangle j. Furthermore, f_i is the integral of the source term f over Ω_i^B, and $\gamma_{i,j,k}$ can be expressed as

$$\gamma_{i,j,k} = \left[\frac{\boldsymbol{K}_{i,j}}{2T_{i,j}} \boldsymbol{\nu}_{i,j,k} \right] \cdot (\boldsymbol{n}_{i,j}^1 + \boldsymbol{n}_{i,j}^2). \tag{5}$$

Here $\boldsymbol{n}_{i,j}^1$ and $\boldsymbol{n}_{i,j}^2$ are the two outward normal vectors (having length equal to the length of the interface) associated with the part of $\partial\Omega_i^B$ lying within triangle j, $\boldsymbol{K}_{i,j}$ and $T_{i,j}$ are the permeability tensor and the area of triangle j, respectively. The vectors $\boldsymbol{\nu}_{i,j,k}$ and the area $T_{i,j}$ results from taking the gradient of the linear pressure variation in triangle j as shown in, e.g., [3].

The last part of the box method consists of the assembly of the coefficient matrix and the right hand side of the linear system for the discrete (vertex) pressures giving N^v linear equations for the N^v unknown vertex pressures $\hat{P}_i$. Note that, for Dirichlét boundary conditions, the number of Dirichlét boundary nodes must be subtracted from N^v, see [37] for a discussion of boundary conditions.

The linear system can be written in matrix form as

$$\boldsymbol{A}\boldsymbol{u} = \boldsymbol{b}, \tag{6}$$

where $\boldsymbol{A}$ is the $N^v \times N^v$ coefficient matrix, $\boldsymbol{u}$ is an $N^v \times 1$ vector of the unknown vertex pressures, and $\boldsymbol{b}$ is an $N^v \times 1$ vector representing the source terms or boundary conditions. Since the linear system is symmetric positive definite, it can be solved rapidly using, e.g., the preconditioned conjugate gradient method.

3.2. **Discrete fractures.** Fractures are approximated using the parallel plate model [12]. In n-dimensional space, fractures are often modeled as $(n-1)$-dimensional objects [27, 58]. In 2D, this means that fractures are associated with the edges of the finite element mesh. Hence, edges are either matrix edges (edges containing no fractures), or fracture edges (edges containing a fracture), see Figure 5 (right). The fracture edges are denoted by $\mathcal{F}_k$, $k = 1, \ldots, N_f$, where N_f is the number of fracture edges. A fracture edge intersects a control volume boundary of the dual mesh at its midpoint, see Figure 5 (right).

Each fracture edge $\mathcal{F}_k$ will also have an associated aperture a_k, permeability k_k, and length l_k. The length l_k is the length of the fracture edge, the permeability k_k is assumed to be isotropic such that a two-point flux can be applied inside the fracture and the aperture a_k is not resolved explicitly in the grid, but used for computing fracture fluxes, as discussed next.

Consider a fracture edge $\mathcal{F}_k$ with end points at nodes $\boldsymbol{\mathcal{V}}_I$, $1 \leq I \leq N^v$, and $\boldsymbol{\mathcal{V}}_J$, $1 \leq J \leq N^v$, as in Figure 5 (right). Then the flux $Q_{i,j,k}$ out of Ω_I^B at the midpoint of $\mathcal{F}_k$ is approximated as a two-point flux

$$Q_k = \frac{k_k a_k}{l_k}(\hat{P}_I - \hat{P}_J). \tag{7}$$

The above fluxes are then taken into account when evaluating the surface integrals resulting from Equation (2), and when assembling the linear system (6).

The lower-dimensional treatment of fractures in the box methods has been popular since it allows for easy mesh generation and a well-conditioned linear systems. However, streamlines cannot be traced directly for this approach, since there is no transversal flow information in the lower-dimensional fractures. It is therefore of interest to consider equi-dimensional methods. In the next section we consider the MPFA method for equi-dimensional fractures. Note that the MPFA method also has been used with lower-dimensional fractures [40], however this approach can only be used for low-permeable fractures.

3.3. **The MPFA O-method.** In cell-centered finite volume methods the control-volumes are associated with the primary grid. This is convenient compared to vertex-centered methods, when considering discontinuous media properties combined with a quadrilateral or triangular primary mesh. In this case it is easy to align the grid edges, and hence, the control-volume boundaries with media discontinuities.

Here we use a multi-point flux O-method (MPFA O-method), briefly described below. For an overview of different MPFA schemes see [2, 1, 3, 28, 67], and references therein. The letter "O" comes from the shape of the polylines connecting the involved grid points in a cell-stensil [2]. The MPFA O-method is based on full flux continuity across cell edges, continuity of the pressure at the midpoint of the cell edges, and mass conservation for each cell. The pressures at cell edges is eliminated locally using the flux continuity constraints, and the global system is expressed in terms of the cell center pressures.

For the MPFA O-method the control volumes are associated with the original mesh, whereas for the box method, control volumes were associated with the dual mesh. By integrating Equation (1) over a control volume Ω_i^M and applying Gauss' theorem we have

$$-\int_{\partial\Omega_i^M} \boldsymbol{K}\nabla P \cdot \boldsymbol{n} dS = \int_{\Omega_i^M} f dV, \qquad i = 1, \ldots, N^e, \tag{8}$$

where $\boldsymbol{n}$ is the unit outward normal vector to $\partial\Omega_i^M$. The only unknown in the last equation is the pressure, which will be approximated at the center of each cell (cell-centered method), in contrast to the Box-method, where the pressure is approximated at the vertices of the grid (vertex-centered method). Hence, Equation (8) gives us N^e equations to determine the N^e unknown cell center pressures. By assuming a constant permeability $\boldsymbol{K}_i$ for each control volume, we can write the integral on the left hand side of

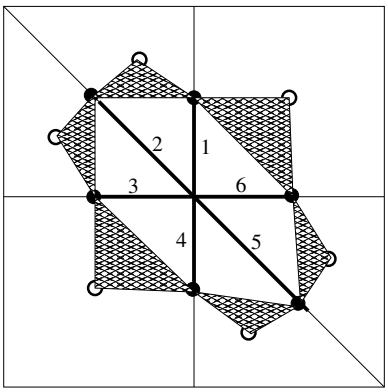

FIGURE 6. An interaction region, variational triangles, half-edges and pressure nodes, respectively, for the central vertex of a simple grid. Variational triangles are cross hatched; the half-edges are the heavy line segments numbered 1-6; solid circles indicate auxiliary (temporary) pressure nodes, and non-solid circles indicate cell center pressures.

Equation (8) as

$$\int_{\partial\Omega_i^M} -\boldsymbol{K}_i \nabla p \cdot \boldsymbol{n} dS = \sum_{j=1}^{N_{e,i}} \int_{\Gamma_{i,j}} -\boldsymbol{K}_i \nabla p \cdot \boldsymbol{n}_{i,j} dS = \sum_{j=1}^{N_{e,i}} Q_{i,j}, \; i = 1, \ldots, N^e, \tag{9}$$

where $N_{e,i}$ is the number of boundary edges of Ω_i^M, i.e., $N_{e,i}$=3 for a triangle and $N_{e,i}$=4 for a quadrilateral, $\Gamma_{i,j}$ is boundary edge number j of Ω_i^M, $\boldsymbol{n}_{i,j}$ is the corresponding outward unit normal vector, and $Q_{i,j}$ is defined by Equation (9). In order to determine the fluxes $Q_{i,j}$ in Equation (9) in terms of the cell center pressures, we use a multi-point flux approximation (MPFA).

The MPFA method is based on dividing the grid into so-called interaction regions $\mathcal{I}_i, i = 1, \ldots, N^v$, associated with each vertex $\boldsymbol{\mathcal{V}}_i$ of the grid. The interaction regions are equal to the control-volumes for the box method, see the previous section. For each interaction region $\mathcal{I}_i$ there is a set of half-edges $E_{i,j}$, see Figure 6. On each side of a half-edge there will be two grid cells, denoted "L" and "R". Furthermore, each interaction region also contains a set of variational triangles $\mathcal{T}_{i,j}^{\alpha}$, $\alpha = L, R$, one for each cell α of half-edge $E_{i,j}$, see Figure 6.

Within each $\mathcal{T}_{i,j}^{\alpha}$, a linear pressure variation is assumed. This is done by fixing the pressure at the corners of each $\mathcal{T}_{i,j}^{\alpha}$. Thus, in addition to the cell center pressures, we introduce (temporary) pressures at the points indicated with the solid circles in Figure 6. The linear pressure in each $\mathcal{T}_{i,j}^{\alpha}$ is now assumed to be valid also for calculating the flow across each of the two half-edges within $\mathcal{I}_i$ that are closest to $\mathcal{T}_{i,j}^{\alpha}$, i.e., those with a common point with $\mathcal{T}_{i,j}^{\alpha}$.

Hence, the pressure gradient will be constant on each side of a half-edge. From Equation (8) we see that the flow rate $\boldsymbol{q}$ must be given as

$$\boldsymbol{q} = -\boldsymbol{K}\nabla P. \tag{10}$$

Substituting the constant pressure gradient into the last equation, we can express the flux across each half-edge $E_{i,j}$ as

$$q_{i,j}^{\alpha} = \sum_{k=1}^{3} t_{i,j,k}^{\alpha} P(\boldsymbol{x}_{i,j,k}^{\alpha}), \tag{11}$$

where

$$t_{i,j,k}^{\alpha} = \frac{|E_{i,j}|}{2T_{i,j}^{\alpha}} \left(\boldsymbol{K}_{i,j}^{\alpha} \boldsymbol{\nu}_{i,j,k}^{\alpha}\right) \cdot \boldsymbol{n}_{i,j}, \tag{12}$$

and $P(\boldsymbol{x}_{i,j,k}^{\alpha})$ is the pressure at corner k of $\mathcal{T}_{i,j}^{\alpha}$. The sign of the unit normal vector $\boldsymbol{n}_{i,j}$ to $E_{i,j}$ is not important, but the same sign must be chosen for each value of α. In the last equation, $|E_{i,j}|$ is the length of $E_{i,j}$; $T_{i,j}^{\alpha}$ and $\boldsymbol{\nu}_{i,j,k}^{\alpha}$ are the area and normal vectors of $\mathcal{T}_{i,j}^{\alpha}$, resulting from taking the gradient of a the linear pressure, see, e.g., [3].

Flux continuity across edge $E_{i,j}$ can now be expressed as $q_{i,j}^{L} = q_{i,j}^{R}$, or

$$A_i \boldsymbol{u}_i + B_i \boldsymbol{v}_i = C_i \boldsymbol{u}_i + D_i \boldsymbol{v}_i, \qquad i = 1, \ldots, N^e, \tag{13}$$

where $\boldsymbol{u}_i$ is a vector of cell center pressures, and $\boldsymbol{v}_i$ contains the auxiliary pressures (which we want to eliminate), and the matrices A_i, B_i, C_i, and D_i, contains the t-coefficients. Note that since the pressure is required to be continuous at the auxiliary pressure nodes, i.e., at the solid circles in Figure 6, there will be only one unknown at these points, and hence each $\boldsymbol{v}_i$ has exactly N_i^E components, where N_i^E is the number of half-edges within $\mathcal{I}_i$. It can also be shown that the matrices B_i and D_i are square $N_i^E \times N_i^E$ matrices.

We here assume that the interaction region $\mathcal{I}_i$ correspond to an interior corner; for boundary corners and implementation of boundary conditions, see [37, 31]. For interior corners, the vectors $\boldsymbol{u}_i$ and $\boldsymbol{v}_i$ will also contain the same number (N_i^E) of unknowns, such that A_i and C_i are also square $N_i^E \times N_i^E$ matrices.

Due to the continuity condition in Equation (13), the flux $q_{i,j}$ across edge $E_{i,j}$ is well defined as either $q_{i,j}^{L}$ or $q_{i,j}^{R}$, and can be expressed as, e.g., $q_{i,j} = q_{i,j}^{L}$, which is expressed in matrix form as

$$\boldsymbol{q}_i = A_i \boldsymbol{u}_i + B_i \boldsymbol{v}_i, \tag{14}$$

where the j-th component $\boldsymbol{q}_i$ is $q_{i,j}$. Finally, we eliminate $\boldsymbol{v}_i$ in Equation (14) by using Equation (13),

$$\boldsymbol{q}_i = (A_i + B_i(B_i - D_i)^{-1}(C_i - A_i))\boldsymbol{u}_i = T_i \boldsymbol{u}_i \tag{15}$$

Since the components of $\boldsymbol{q}_i$ represents fluxes over half edges adjacent to a given corner $\boldsymbol{\mathcal{V}}_i$, the flux over edge $\Gamma_{k,j}$ of grid cell Ω_k^M (see Equation (9)) can be found be combining certain components $\boldsymbol{q}_i$, $i = A, B$, where $\boldsymbol{\mathcal{V}}_A$ and $\boldsymbol{\mathcal{V}}_B$ are the end points of $\Gamma_{k,j}$.

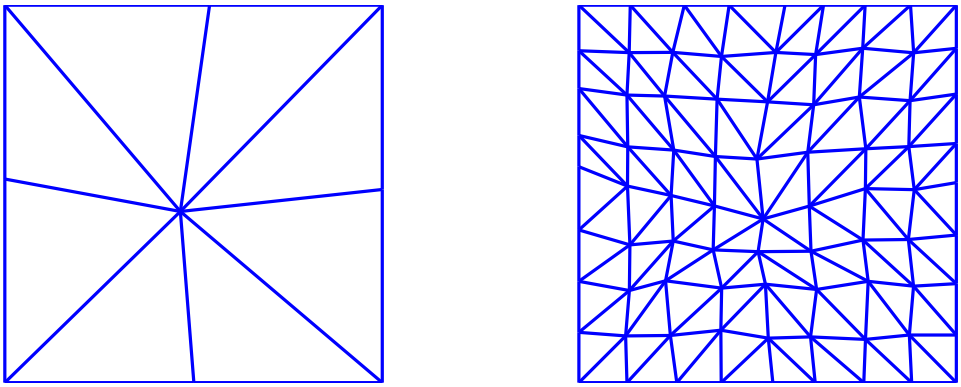

FIGURE 7. Left: Initial grid. Right: Level 2 refined grid.

In this way, we assemble expressions for each of the $Q_{i,j}$ in Equation (9) and inserting these into (8), we obtain N^e linear equations that can be solved for the N^e unknown cell center pressures. The linear system is expressed as

$$A\boldsymbol{u} = \boldsymbol{b}, \tag{16}$$

where A is the $N^e \times N^e$ coefficient matrix, $\boldsymbol{u}$ is an $N^e \times 1$ vector of the unknown cell center pressures, and $\boldsymbol{b}$ is an $N^e \times 1$ vector representing the source terms for each Ω_k^M, $k = 1, \ldots, N^e$, see Equation (8).

4. Numerical experiments

In this section we solve Equation (1) numerically, using the box method and the MPFA method.

4.1. **Homogeneous case.**

We first consider the homogeneous case with no fractures. By investigating this simple case first, we will get a feeling of how the methods perform, including the sensitivity of the solution to different boundary conditions and to grid perturbation, before extending to the more complex cases including fractures.

Assume $\boldsymbol{K} \equiv 1$, no source terms ($f \equiv 0$), and Dirichlet boundary conditions in a domain $\Omega = [0, 2] \times [-1, 1]$. The boundary conditions were imposed by one of three different analytical solutions,

$$P_1(x, y) = x^2 - y^2 + xy + x + y + 1, \tag{17}$$

$$P_2(x, y) = x^3 - 3xy^2 + 3x^2y - y^3 + x^2 - y^2 + xy + x + y + 1, \tag{18}$$

$$P_3(x, y) = \cos(x)\cosh(y). \tag{19}$$

The influence of the following boundary conditions were investigated:

- Type 1: Dirichlét boundary conditions on the whole boundary,
- Type 2: Neumann boundary conditions on the whole boundary, and the pressure fixed at an interior point, and
- Type 3: Mixed boundary conditions, with Neumann boundary conditions at the top and bottom, and Dirichlét at the left and right boundary.

The convergence tests were performed on a sequence random grids, starting with the coarsest grid, as shown in Figure 7 (left). Five refinement levels was

TABLE 1. Convergence rates for pressure and flux in terms of DOFs.

	MPFA1	MPFA2	MPFA3	BOX1	BOX2	BOX3
	Pressure					
P_1	-.96	-1	-.99	-.91	-1	-.93
P_2	-.97	-1	-.99	-.91	-1	-.97
P_3	-.97	-.94	-.99	-.95	-1	-.97
	Flux					
P_1	-.57	-.52	-.52	-.46	-.49	-.47
P_2	-.57	-.5	-.5	-.47	-.49	-.48
P_3	-.58	-.49	-.5	-.47	-.49	-.48

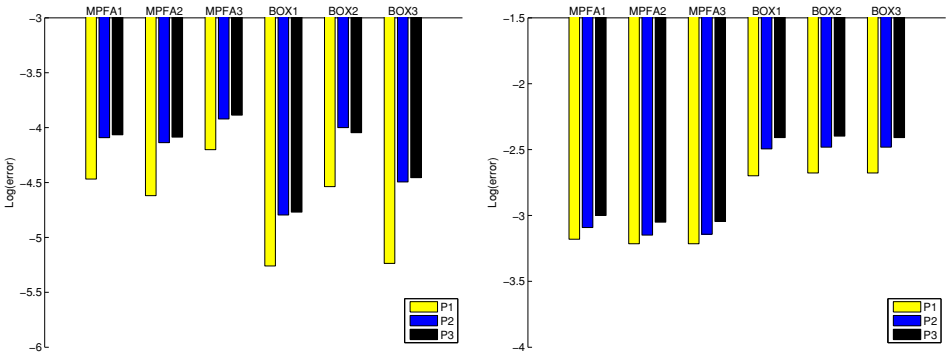

FIGURE 8. Accuracy at 3950 DOFs obtained by interpolating between the two closest grids. Left: Pressure. Right: Flux.

considered; each refinement was obtained by splitting each triangle of the original grid into four sub triangles, leading to a refined grid with four times as many cells as the original. Then each grid vertex was given a random perturbation. The level 2 refined grid is shown in Figure 7 (right). The smallest angle of any element were 36, 32, 24, 18, 14, and 9 degrees, for the coarsest to the finest grid.

The convergence rates for pressure and flux based on the discrete L^2 error [31] are shown in Table 1. The number after the method name refers to the boundary condition, e.g., MPFA1 is the MPFA method using boundary condition of type-1. Note that the MPFA method has more degrees of freedom (DOFs) than the box method for the same grid, since we use a triangular grid and the MPFA method is a cell-cent red method, whereas the box method is vertex-centered. We therefore display convergence results as a function of the DOFs; the convergence rate in terms of the mesh size parameter h can be obtained approximately by a multiplication by -2.

The results in Table 1 are in agreement with the theoretical results presented in the literature for the box method [32] and for the MPFA method [47]. The results show a second order convergence in pressure and first order in flux.

The accuracy at 3950 DOFs are shown in Figure 8. The results show that

TABLE 2. Runtime in seconds per degree of freedom (R.T./DOF) for each method as a function of grid refinement level.

		$\mathcal{G}_0$	$\mathcal{G}_1$	$\mathcal{G}_2$	$\mathcal{G}_3$	$\mathcal{G}_4$	$\mathcal{G}_5$	$\mathcal{G}_6$
R.T./DOF	BOX	0.04	0.0044	0.0027	0.0024	0.0024	0.0025	0.0032
	MPFA	0.0025	0.0031	0.0027	0.0027	0.0028	0.0038	0.014

the MPFA method is most accurate for flux, and the BOX method is most accurate for the pressure.

As noted in Section 3.1, the system matrix for the box method is symmetric and positive definite, and we used a Cholesky factorization to solve the corresponding linear system. An other alternative would be the preconditioned conjugate gradient method, see [25] for a comparison. The system matrix for the MPFA method is, however, not symmetric [30], and the UMFPACK [26] LU-factorization is used for this system. Table 2 shows runtimes for the methods obtained for the Dirichlét boundary condition. The runtimes are divided by the degrees of freedom to provide a fair comparison between the methods. Note also that an extra refinement level, $\mathcal{G}_6$, is included in the table. The number of elements for $\mathcal{G}_i$, $i = 0, \ldots, 6$ was 8×4^i, respectively. Hence $\mathcal{G}_6$ contained 32768 elements. The table shows that the runtime per degree of freedom is almost constant for the box method for refinement levels 3, 4, and 5, and then starts to increase slightly for the last refinement level. For the MPFA method, the runtime is almost constant for first 4 refinement levels, and then starts to increase. For the last refinement ($\mathcal{G}_6$), the box method is approximately 4 times faster than the MPFA method.

The numerical test in this section indicates that:

- For fine grids (more than 20000 DOFs), the box method will be faster the MPFA method;
- The box method is most accurate for the pressure, whereas the MPFA method is most accurate for the flux;
- The convergence rate of the MPFA method and the box method were similar for both flux and pressure.

4.2. **Single fracture.** In this section we solve Equation (1) for the case where the permeability tensor $\boldsymbol{K}$ is assumed to be the piecewise constant scalar,

$$\boldsymbol{K}(x,y) = \begin{cases} 1, & (x,y) \in \Omega_1 \\ k_F, & (x,y) \in \Omega_2 \\ 1, & (x,y) \in \Omega_3. \end{cases} \tag{20}$$

The solution domain $\Omega = \Omega_1 \cup \Omega_2 \cup \Omega_3$ is shown in Figure 9 (left). The domain Ω_2 will act as a single horizontal fracture with aperture ϵ.

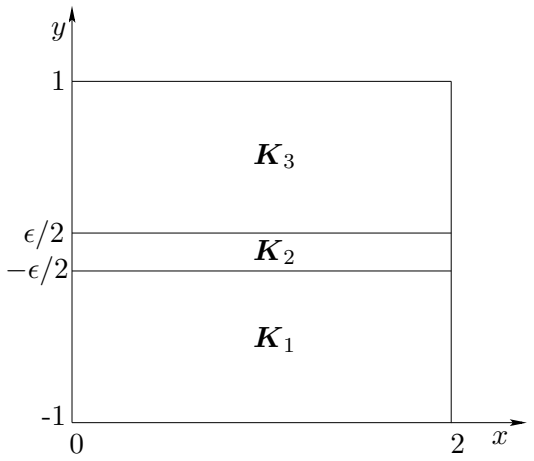

FIGURE 9. A domain with a single horizontal fracture.

We will consider the following analytical solution,

(21)
$$P_F(x,y) = \begin{cases} k_F \cos(x)\cosh(y) + (1-k_F)\cosh(\epsilon)\cos(x) & (x,y) \in \Omega_1 \\ \cos(x)\cosh(y) & (x,y) \in \Omega_2 \\ k_F \cos(x)\cosh(y) + (1-k_F)\cosh(\epsilon)\cos(x) & (x,y) \in \Omega_3, \end{cases}$$

where the source term in Equation (1) is given by

(22)
$$f(x,y) = \begin{cases} (1-k_F)\cosh(\epsilon)\cos(x), & (x,y) \in \Omega_1 \\ 0, & (x,y) \in \Omega_2 \\ (1-k_F)\cosh(\epsilon)\cos(x), & (x,y) \in \Omega_3. \end{cases}$$

The boundary conditions will be determined by the analytical solution, and we consider the type-1, type-2, and type-3 boundary conditions as described in the previous section.

The numerical solution is computed in five different ways. First, we represent the fracture in Figure 9 using a lower dimensional object, i.e., a horizontal line segment at y=0. This method will be denoted the BOXL ("L" for lower-dimensional) method. The other four methods are based on the equi-dimensional representation of the fracture. As discussed in Section 2, the equi-dimensional fractures are obtained by expanding the fracture *after* the domain has been triangulated. Two alternatives are investigated. The first uses quadrilateral elements in the fracture. This is shown in Figure 10 (left) for the coarsest grid and for an exaggerated fracture aperture. Using this grid, we solve the pressure equation using both the MPFA method and the box method, leading to the methods BOXQ and MPFAQ ("Q" for quadrilateral). The last alternative uses triangular elements in the fracture, shown in Figure 10 (right), leading to the methods BOXT and MPFAT.

However, as it turned out that the errors for the methods using triangular elements in the fracture could not be distinguished visually from the errors of the same method using quadrilateral elements in the plots presented below. Hence, to simplify the presentation, we do not display any results for BOXT and MPFAT methods in the following.

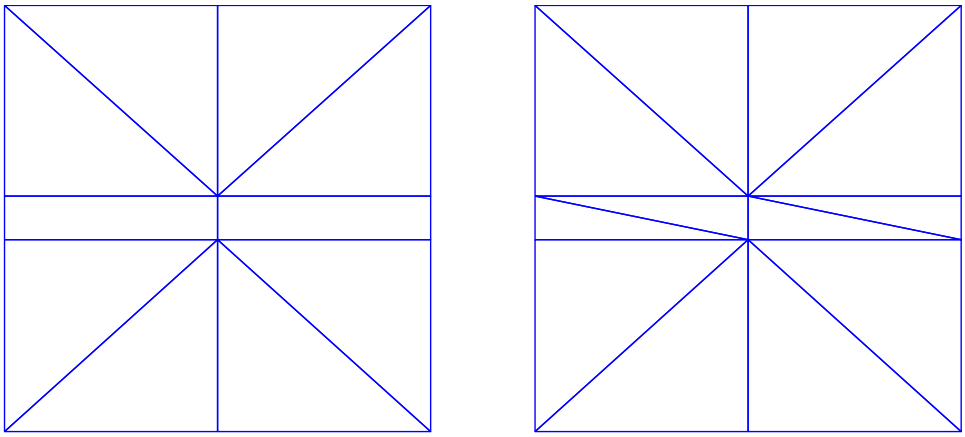

FIGURE 10. Different discretizations of an expanded fracture. The aperture of the horizontal fracture at the center of the domain is exaggerated for illustration purposes. Left: Quadrilateral elements in the fracture. Right: Triangular elements.

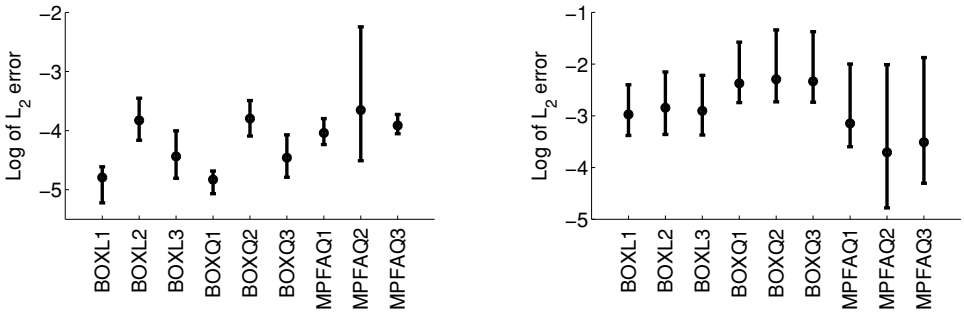

FIGURE 11. Errorbar plot for the L^2 error in pressure at 3950 DOFs. Left: Pressure. Right: Flux

We would like to investigate both the influence of the thickness of fracture, and the influence of the permeability contrast between the fracture and the matrix on the system behavior. However, in a later section we show that these two factors are not independent in their influence on the condition number of the system. We have therefore chosen to investigate only the permeability contrast here. Then, in order to include a range of both low-permeable fractures and high-permeable fractures we consider the following cases for the fracture permeability:

$$k_{F,i} = 10^{i-6}, \qquad i = 1, 2, \ldots, 11, \tag{23}$$

and we chose to fix the fracture fracture aperture to

$$\epsilon = \text{1e-4} \tag{24}$$

for all cases.

The results for accuracy are shown in Figure 11. As in the previous section, we evaluate the accuracy at 3950 DOFs, and the last figure in the

TABLE 3. Convergence rates for pressure in terms of DOFs. Note that the rates for the BOXQ1, BOXQ3, MPFAQ1, and MPFAQ3 are not included in the table below since they were -1 for all cases of the fracture permeability.

Perm.	BOXL1	BOXL2	BOXL3	BOXQ2	MPFAQ2
1e-05	-0.99	-1.1	-1	-0.9	-0.5
1e-04	-0.99	-1.1	-1	-0.92	-0.49
1e-03	-0.99	-1.1	-1	-0.92	-0.53
1e-02	-0.99	-1.1	-1	-0.92	-0.99
1e-01	-1	-1.1	-1	-0.91	-1.1
1e+00	-1.3	-0.91	-0.92	-1	-1
1e+01	-0.75	-0.92	-0.91	-1	-1
1e+02	-0.76	-0.93	-0.91	-1	-1
1e+03	-0.75	-0.96	-0.92	-1	-1
1e+04	-0.78	-0.99	-0.95	-1	-1
1e+05	-1	-1	-1	-0.99	-1

method names gives the type of boundary condition used, e.g., BOXL1 corresponds to the BOXL methods using boundary conditions of type 1.

The bars on the accuracy plots are obtained by considering the different results for each $k_{F,i}$, $i = 1, \ldots, 11$. The central points on the errorbars correspond to the average over all $k_{F,i}$, and the extrema on the bars corresponds to the minimum and maximum value over all $k_{F,i}$. The results show again that the box method is the most accurate for pressure, whereas the MPFA method is most accurate for the flux. However, there are relatively large variation over the different fracture permeabilities.

The convergence rate for pressure was second order (-1 in DOFs) for the BOXQ1, BOXQ3, MPFAQ1, and MPFAQ3 methods. However, for the other methods the convergence rate depended on the fracture permeability as shown in Table 3.

The convergence rates for flux are shown in Table 4. All the BOXL methods showed a similar behavior; we only show the BOXL2 method in Table 4. The BOXQ methods showed a similar behavior as the BOXQ2 method in Table 4, and all the MPFAQ methods all showed different behavior, also see Table 4.

4.3. **Accuracy of the BOXL method.** Note that the convergence rates for the BOXL method in Tables 3 and 4 were obtained at the last, i.e. fifth, refinement level of the grids in Figure 10. For this grid the error in the BOXL method was larger than approximately 1e-5. However, for finer grids we observed a lack of convergence for the BOXL method. The convergence for the BOXL method ceased when the errors got smaller than approximately 1e-5.

To explain this, we consider the square domain of size $d \times d$ in Figure 12. For a homogeneous scalar permeability $\boldsymbol{K}(x, y) = 1$ the flux stencil for the central vertex in the figure (corresponding to mass conservation for the

TABLE 4. Convergence rates for flux in terms of DOFs. Convergence rates for the BOXL1, BOXL3, BOXQ1, and BOXQ3 methods are not shown here, but discussed in the main text.

Perm.	BOXL2	BOXQ2	MPFAQ1	MPFAQ2	MPFAQ3
1e-05	-0.75	-0.51	-0.94	-0.71	-0.85
1e-04	-0.75	-0.51	-0.94	-0.71	-0.85
1e-03	-0.75	-0.51	-0.93	-0.71	-0.83
1e-02	-0.75	-0.51	-0.94	-0.73	-0.86
1e-01	-0.75	-0.51	-0.94	-0.74	-0.88
1e+00	-0.76	-0.51	-0.93	-1	-1
1e+01	-0.76	-0.52	-0.93	-0.77	-0.84
1e+02	-0.91	-0.71	-0.87	-0.9	-0.83
1e+03	-1.4	-1.2	-0.95	-1	-0.96
1e+04	-1.4	-1.3	-0.99	-1	-1
1e+05	-1.3	-1.3	-0.99	-1	-1

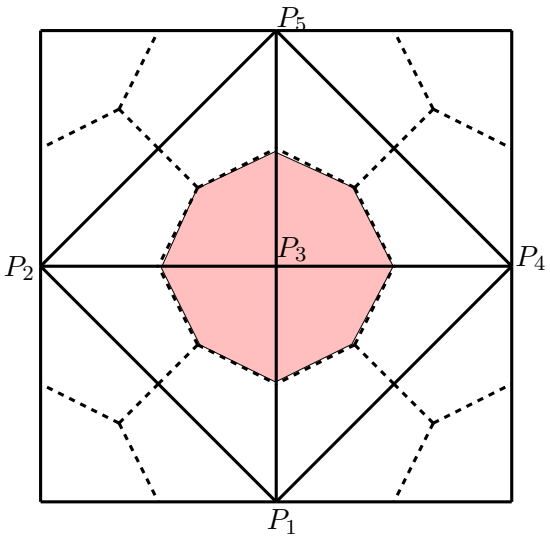

FIGURE 12. A square domain of size $d \times d$, discretized with 8 triangles.

shaded control volume) is given by

$$-P_1 - P_2 + 4P_3 - P_4 - P_5 = 0. \tag{25}$$

Consider now a horizontal (lower dimensional) fracture of aperture ϵ extending from P_2 to P_4 in the figure. Let the permeability of the fracture be $k_F = 1$. Then the flux stencil for the BOXL method becomes

$$-P_1 - (1 + \frac{2\epsilon}{d})P_2 + (4 + \frac{4\epsilon}{d})P_3 - (1 + \frac{2\epsilon}{d})P_4 - P_5 = 0.$$

The introduction of the additional terms in the last equation, introduces an error of size $\mathcal{O}(\epsilon/d)$ into the system matrix for the BOXL method. This error is not reduced as the grid is refined, and explains why the BOXL cannot converge.

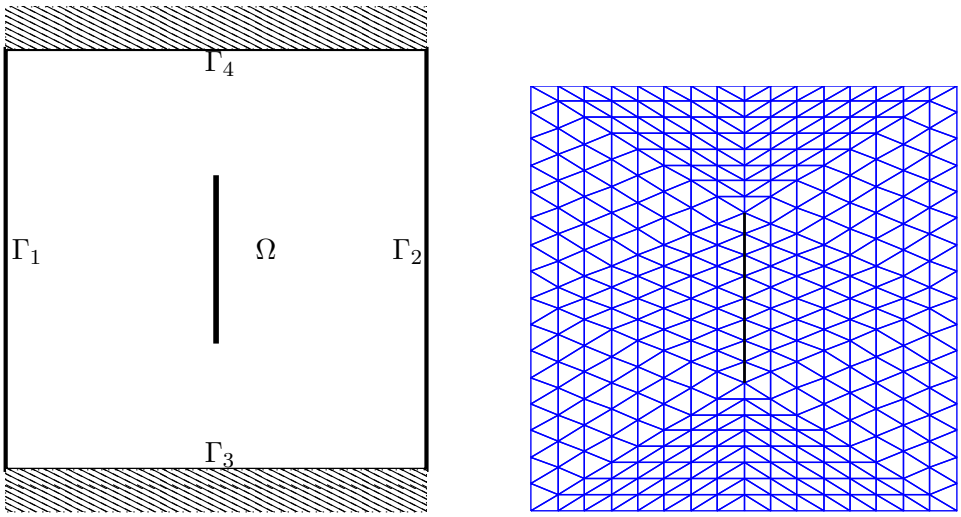

FIGURE 13. Left: A square domain with a vertical fracture. Right: Initial discretization (Ref0) of the domain to the left.

4.4. **Low-permeable fractures.** In this and the following sections, we will use boundary conditions of type-3, but they will not be determined from an analytical solution as in the previous sections, rather we solve the following problem:

$$\nabla \cdot (\boldsymbol{K} \nabla P) = 0, \qquad \text{in } \Omega \tag{26a}$$

$$P = 1, \qquad \text{on } \Gamma_1 \tag{26b}$$

$$P = 0, \qquad \text{on } \Gamma_2 \tag{26c}$$

$$(\boldsymbol{K} \nabla P) \cdot \boldsymbol{n} = 0, \qquad \text{on } \Gamma_3 \cup \Gamma_4. \tag{26d}$$

The domain $\Omega = [0,1] \times [0,1]$ is shown in Figure 13 (left). The boundary of the domain consists of the union of the four straight lines, Γ_i, $i = 1, \ldots, 4$, shown in Figure 13 (left).

We will assume that the permeability tensor is a piecewise constant scalar given as

$$\boldsymbol{K}(\boldsymbol{x}) = \begin{cases} k_M, & \boldsymbol{x} \text{ in matrix,} \\ k_F, & \boldsymbol{x} \text{ in fractures} \end{cases} \tag{27}$$

We will show that the BOXL method should not be used when fractures are barriers to flow, i.e. for the case $k_F < k_M$. Consider a vertical fracture (drawn in black) located in the center of the domain, see Figure 13 (right). We will assume a matrix permeability of k_M=1, and the fracture permeability $k_F < 1$. The the domain is discretized as shown in Figure 13 (right), and a fracture width of ϵ=1e-4 is assumed. We first solve Problem (26) with the MPFAQ method, using a fracture permeability of k_F=1e-10. The result is shown in Figure 14 (left). Here we have traced 40 streamlines for the pressure solution. Refer to [38] for details about the streamline tracing algorithm. We see that the flow correctly avoids the barrier. We now solve the same problem using the BOXL method. The result is shown in Figure 14 (right). We see that the barrier is not respected by the box solution. The

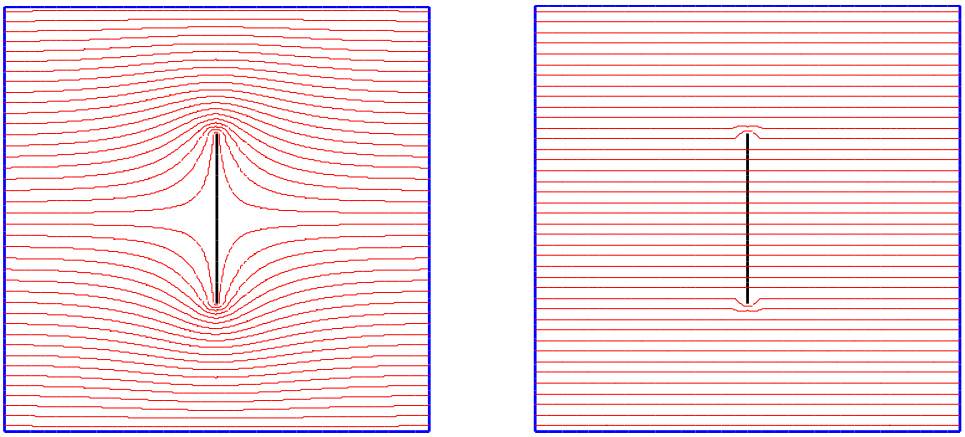

FIGURE 14. Streamlines in a domain with a low permeable vertical fracture. Left: MPFAQ method, Right: BOXL method

streamlines penetrates the barrier as it did not exist. Note that in order to trace streamlines with the box solution, a flux recovery procedure was used, see [38] for details.

The behavior of the box method can be explained by considering Figure 12. Assume first a homogeneous domain, i.e. $k_F = k_M = 1$. Then the flux stencil for the central vertex in the figure is given by Equation (25) Consider now a vertical fracture of aperture ϵ extending from P_1 to P_5 in the figure. Let the permeability of the fracture be k_F, and the permeability of the matrix be k_M=1. Then the flux stencil for the box method becomes

$$-P_2 - (1 + \frac{2k_F\epsilon}{d})P_1 + (4 + \frac{4k_F\epsilon}{d})P_3 - (1 + \frac{2k_F\epsilon}{d})P_5 - P_4 = 0.$$

As k_F approaches zero, the last expression approaches Equation (25). Hence, the influence of a low permeable fracture ($k_F < k_M$) on the flow behavior will be neglected by the box method, see Figure 14 (right).

We note that the type of boundary conditions can make the error in the BOXL method less noticeable. This can be seen in the results from Section 4.2 in Tables 3 and 4. Here, it seems like the BOXL method converges for the low permeable cases. However, the behavior of the system is here dominated by the boundary conditions, and the true solution does not change significantly from the homogeneous case to the case where k_F=1e-5.

4.5. **Investigation of the condition number.** The condition number of a matrix $\boldsymbol{A}$ is defined as

$$\kappa = \|\boldsymbol{A}\|\|\boldsymbol{A}^{-1}\|,$$

where the norm is usually taken to be the 2-norm. The condition number is important due to its relation to the propagation of round-off errors and to the convergence rate of an iterative solver [36, 39, 63].

In our case, the condition number of the system matrix resulting from discretizing the problem in Equation (26a), depends on many factors. Firstly, the condition number depends on the number of degrees of freedom (DOFs)

TABLE 5. Number of unknowns and condition number for each method as a function of grid refinement level.

		Ref0	Ref1	Ref2	Ref3	Ref4	Ref5
DOF	BOX	3	15	63	255	1023	4095
	MPFA	8	32	128	512	2048	8192
COND	BOX	3.7	15	58	220	855	3371
	MPFA	9	31	120	479	1919	7683

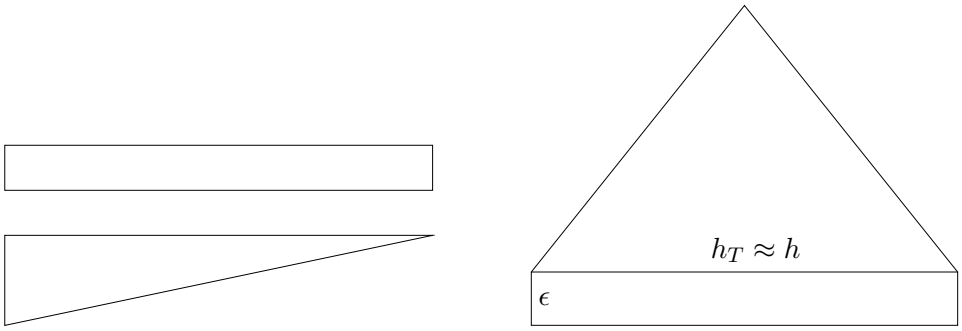

FIGURE 15. Left: A "thin" rectangle and a triangle with a small angle. Such "thin" elements tend to cause ill-conditioned systems. Right: Illustration of the parameters ϵ and h. Two elements from a larger grid are shown. The triangle is a matrix element, and the rectangle is a fracture element. The side length h_T of the triangle is approximately the same size as h. Note that h_T is equal to the "length" of the fracture element.

in the solution. To illustrate this, consider the case of a homogeneous domain with no fractures and permeability $\boldsymbol{K} \equiv 1$. A sequence of grids with increasing DOFs is obtained starting with a grid similar to that shown in Figure 7 (left). The refinements are obtained in the same way as explained in Section 4.1, without random perturbation of the corners. The results for the condition number in Table 5 reveal an almost exact linear relation on the form

$$\kappa = aN + b,$$

where N is the number of degrees of freedom, and a and b are constants. A least-square fit to the data shows that $a \approx .822$ for the box method, $a \approx 1.10$ for the MPFA method.

In equi-dimensional fracture models, "thin" elements (see Figure 15 (left)) typically occur in the fracture. It is well known that for triangular grids, small angles tend to produce a high condition number. For quadrilaterals, "thin" elements, e.g. a rectangle with one side length much larger than the other side length, may also cause problems. A common way to eliminate "thin" elements is to use adaptive grid refinement. Drawbacks of the adaptive method may be an increased number of unknowns, and more difficult mesh generation. In this paper we will not consider the adaptive method further.

The fracture aperture ϵ and the grid size parameter h are illustrated in Figure 15 (right). Note that for a coarse mesh, we typically have $h \gg \epsilon$, and the elements in the fractures tend to be very "thin". However, as the grids are refined and ϵ is kept fixed, h will approach ϵ in size, and the fracture elements will become more and more regular in shape. This effect tends to reduce the condition number, but since the condition number also increase with the number of degrees of freedom, or with the grid refinement level, there is a trade-off here.

The parameters h and ϵ, are not independent in their influence on the condition number. If $h \gg \epsilon$ the condition number only depends on the single parameter $\alpha = h/\epsilon$ (all other parameters held fixed). This is also true for the fracture permeability k_F and the matrix permeability k_M, which can be substituted for by the single parameter $\beta = k_F/k_M$. At last, it was found that for the box method all of the previous parameters could be substituted for by the single parameter

$$\gamma = \frac{hk_F}{\epsilon k_M}$$

Hence the influence of the different parameters on the condition number for a given grid $\mathcal{G}$ can be summarized as

$$\kappa = \begin{cases} f_M^{\mathcal{G}}(\gamma, N), & M\text{=BOXL, BOXQ, BOXT} \\ f_M^{\mathcal{G}}(\alpha, \beta, N), & M\text{=MPFAQ, MPFAT} \end{cases} \tag{28}$$

for an unknown function $f_M^{\mathcal{G}}$ and number of degrees of freedom N. Here $\mathcal{G}$ refers to a grid with a particular fracture configuration.

To sum up, if we also allow the grid parameter $\mathcal{G}$ to vary, the following factors may have an influence on the condition number:

- the parameters α, β, and γ
- number of fractures
- number of crossing fractures,
- fractures ending at the boundary of the domain, and
- how fracture endpoints are discretized.

In theory, the effects of each parameter on the condition number could be determined by looking at the coefficient matrix $\boldsymbol{A}$ and how parameters enter the matrix, and relations between the different elements. However, using this approach we were only able to discover the general relation in Equation (28); the form of the function $f_M^{\mathcal{G}}$ in that equation could only be determined from extensive numerical simulations for given fracture configuration $\mathcal{G}$ and selected values of the parameters α, β and γ.

The influence of β and γ is in the following investigated by changing the fracture permeability k_F. We consider 14 different test cases, as shown in Figure 16, corresponding to different number of fractures crossing each other at a point. For each grid we solve Equation (26a), with $k_M \equiv 1$. We also tried to improve the condition number for the MPFA method by using a simple diagonal scaling preconditioner. The scaling was done by dividing each row of the system matrix by the maximum element in absolute value in that row (typically the diagonal element). The effect of the scaling is to normalize the coefficient matrix, which may be efficient in the case where

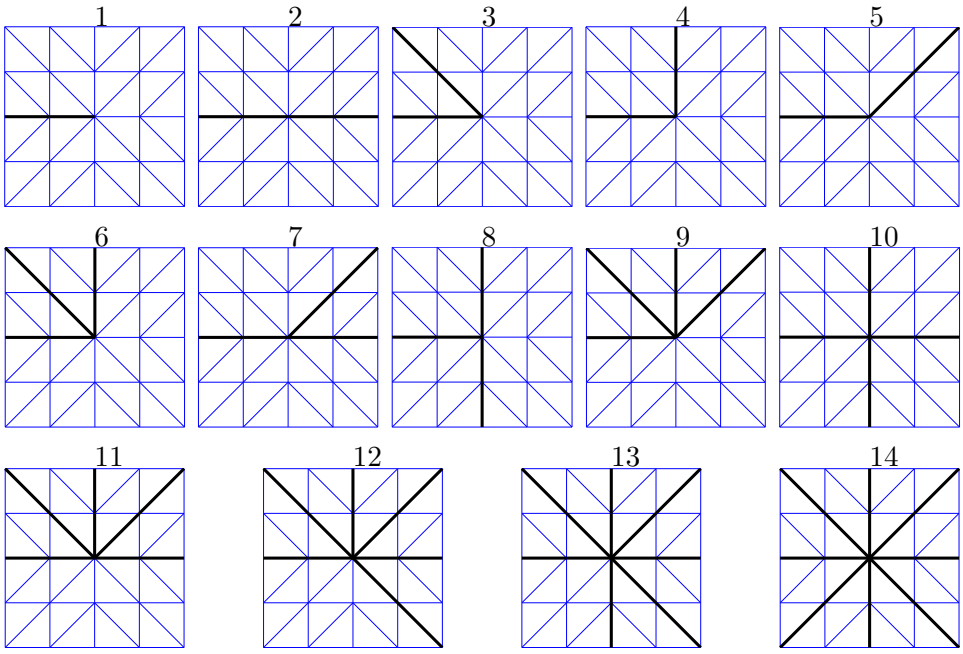

FIGURE 16. 14 different test cases.

the elements of each row considered separately are of approximately the same magnitude, but at the same time, relatively large differences between different rows exists. In order to keep the symmetry, the system matrix of the box method was not scaled.

The results for the condition number as a function of fracture permeability is shown in Figure 17. In the test, the grids in Figure 16 were refined one level, such that the DOFs of the box methods were approximately 65, and the number of degrees of freedom for the MPFA methods were around 130. It was found that the condition number for the BOXQ and BOXT methods could not be distinguished visually on the figures. Hence, the condition number of these methods are represented by the BOXE (box equi-dimensional) curve in the figure. Also, several of the cases showed very similar behavior for the condition number, e.g., case-1 and case-2 were similar, and are represented by the single subfigure with title "case1-2". In addition, the condition number for the BOXL method is only calculated for the cases $k_F > k_M = 1$, due to its deficiency for the low permeable cases, confer with the discussion in Section 4.4.

The test showed that the condition number for the BOXE and BOXL methods for all cases increased steadily with fracture permeability when fracture permeability was larger than approximately 10^{-3}, see Figure 17. For low fracture permeability, the condition number was low for all equi-dimensional methods for cases 1-5, cases 7-8, and case 10. The MPFA methods had low condition number for all the high-permeable cases. We also note that the BOXL method was better conditioned than the BOXE method for all the high-permeable cases.

4.6. **Convergence study for a synthetic test case.** In this section we show how the methods perform on a more realistic test case. We compare

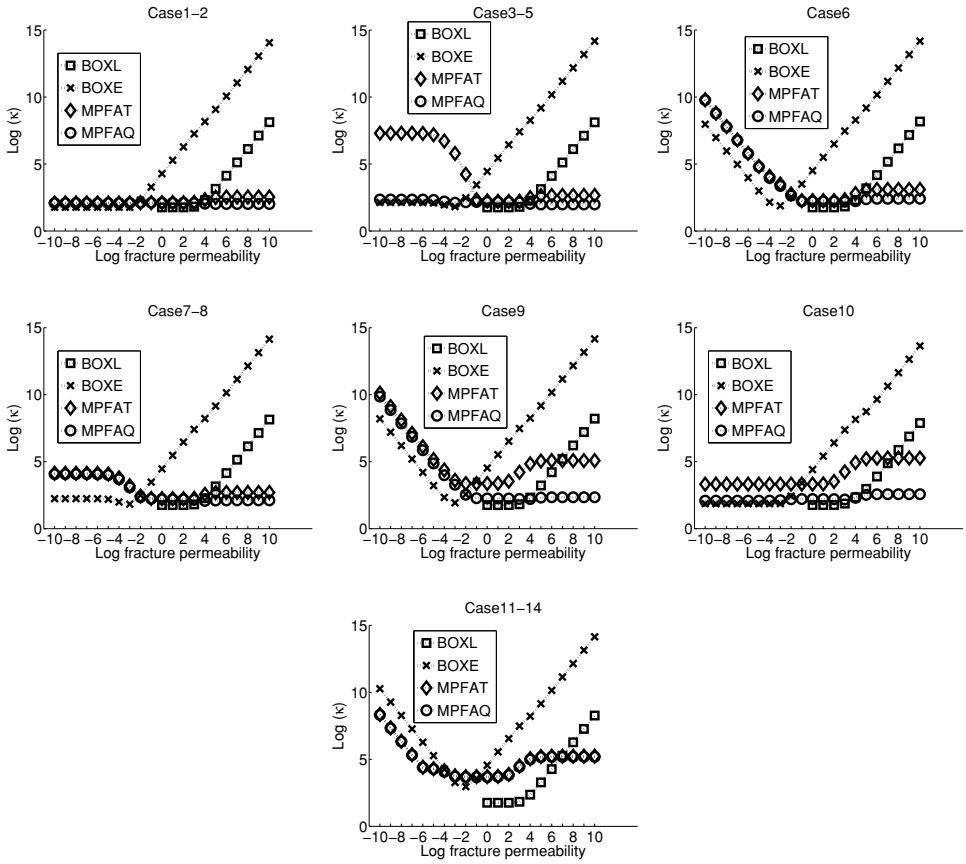

FIGURE 17. The condition number for the 14 different test cases.

the BOXL method and the MPFAQ method on a coarse and a fine grid of a fracture realization, see Figure 18 (top). The coarse grid consist of 163 elements, and the fine grid has 8211 elements. We solve the boundary problem given in Equation (26), and use a fracture permeability of $k_F = 10^3$, a matrix permeability of $k_M \equiv 1$, and a fracture aperture of $\epsilon = 10^{-4}$.

A number of 40 streamlines was traced for each method on each grid. The streamlines for the BOXL method are red, and streamlines for the MPFAQ method are black. The streamlines are distributed uniformly on the left hand edge according to the inflow flux, and hence started at exactly the same points for each method.

We see that the streamlines converge as the grid is refined.

5. Summary and conclusions

In this paper we have compared discretization methods for a discrete fracture model in 2D. Two conceptually different finite volume methods were considered for the pressure equation: A vertex-centered box method based on a Donald-mesh, and a cell-centered MPFA O-method. We considered accuracy and numerical convergence of flux and pressure for homogeneous

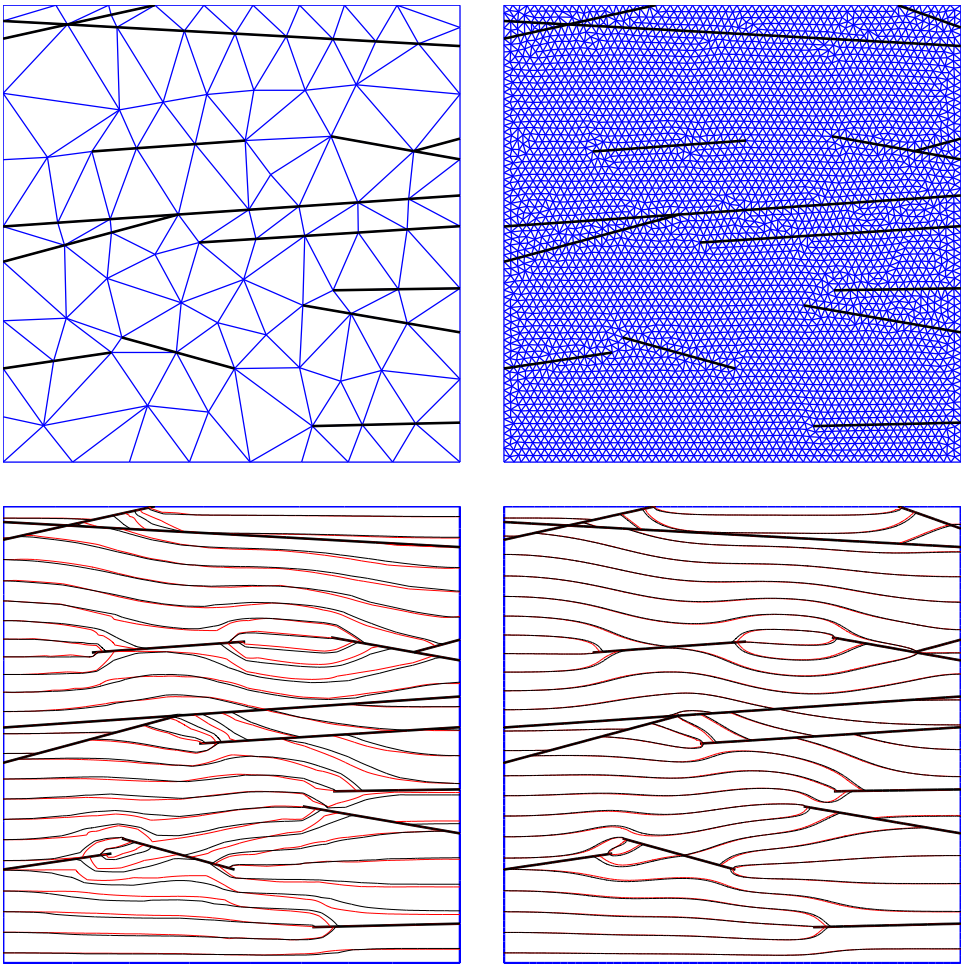

FIGURE 18. Grids and streamlines for the synthetic test case. Top Left: Coarse grid. Top Right: Fine grid. Bottom Left: Streamlines for the coarse grid. Bottom Right: Streamlines for the fine grid.

and fractured systems. In addition, the effects of fracture aperture, permeability contrast, and number of crossing fractures, on the condition number were investigated.

The MPFA method used an equi-dimensional treatment of the fractures, whereas the box method was tested with both lower-dimensional and equi-dimensional fractures. A procedure for expanding a lower dimensional discrete fracture-model to an equi-dimensional model was proposed.

The box methods produced a symmetric positive definite matrix, which enabled a fast and efficient solution of the corresponding linear system. The MPFA method produced an asymmetric matrix which excluded the use of high-efficient solvers. The box method were in general the most accurate methods for the pressure, whereas the MPFA-methods were the most accurate methods for the flux variable.

The lower-dimensional box method could only be used for high-permeable fractures. Also, this method could not achieve high-accuracy results, due

to the simplified treatment of the fractures. However, for most cases, the high-accuracy deficiency will probably not be an issue due to coarse meshes or other more important errors.

Several relations between different parameters in the fracture model, and the condition number was found. The numerical tests indicated that the MPFA-methods have well-behaved condition number for the case of high-permeable fractures in low-permeable matrix.

Acknowledgment. This work was supported by the International Research Training Group "Non-Linearities and Upscaling in Porous Media (NUPUS)" financed by the German Research Foundation (DFG).

References

[1] I. Aavatsmark. An introduction to multipoint flux approxmations for quadrilateral grids. *Comput. Geosci.*, 6:405–432, 2002.

[2] I. Aavatsmark, T. Barkve, Ø. Bøe, and T. Mannseth. Discretization on unstructured grids for inhomogeneous, anisotropic media. part i: Derivation of the methods. *SIAM Journal of Scientific Computing*, 19(5):1700–1716, 1998.

[3] I. Aavatsmark and G.T. Eigestad. Numerical convergence of the MPFA O-method and U-method for general quadrilateral grids. *Int. J. Numer. Meth. Fluids*, 51:939–961, 2006.

[4] P.M. Adler and J.-F. Thovert. *Fractures and fracture networks*, volume 15 of *Theory and applications of transport in porous media*. Kluwer Academic Publ., Boston, 1999.

[5] T. Arbogast, C.N. Dawson, P.T. Keenan, M.F. Wheeler, and I. Yotov. Enhanced cell-centered finite differences for elliptic equations on general geometry. *SIAM J. Sci. Comput.*, 19(2):404–425, 1998.

[6] T. Arbogast, M.F. Wheeler, and I. Yotov. Mixed finite elements for elliptic problems with tensor coefficients as cell-centered finite-differences. *SIAM J. Numer. Anal.*, 34(2):828–852, 1997.

[7] D.N. Arnold, D. Boffi, and R.S. Falk. Quadrilateral H(div) finite elements. *SIAM J. Numer. Anal.*, 42(6):2429–2451, 2005.

[8] A. Assteerawatt, R. Helmig, H. Hægland, A. Bárdossy, and H.K. Dahle. Simulation of flow and transport processes in a discrete fracture-matrix system. i. geostatistical generation of fractures on an aquifer analogue scale. Submitted to *Water Resources Research*, 2008.

[9] B.R. Baliga and S.V. Patankar. A new finite-element formulation for convection-diffusion problems. *Numerical Heat Transfer*, 3:393–409, 1980.

[10] R.E. Bank and D.J. Rose. Some error estimates for the box method. *SIAM J. Numer. Anal.*, 24(4):777–787, 1987.

[11] J.A. Barker. Transport in fractured rock. In R.A. Downing and W.B. Wilkinson, editors, *Applied groundwater hydrology*, Oxford science publications, pages 199–216. Clarendon Press, Oxford, 1991.

[12] J. Bear. Modeling flow and contaminant transport in fractured rocks. In J. Bear, C.-F. Tsang, and G. de Marsily, editors, *Flow and contaminant transport in fractured rock*, pages 1–37. Academic Press, San Diego, 1993.

[13] M. Belayneh, S. Geiger, and S.K. Matthäi. Numerical simulation of water injection into layered fractured carbonate reservoir analogs. *AAPG Bulletin*, 90(10):1473–1493, 2006.

[14] B. Berkowitz. Characterizing flow and transport in fractured geological media: A review. *Adv. Water Resour.*, 25:861–884, 2002.

[15] E. Bonnet, O. Bour, N.E. Odling, P. Davy, I. Main, P. Cowie, and B. Berkowitz. Scaling of fracture systems in geological media. *Reviews of Geophysics*, 39(3):347–383, 2001.

[16] F. Brezzi and M. Fortin. *Mixed and hybrid finite element methods*. Springer series in computational mathematics, 15. Springer-Verlag, New York, 1991.

[17] Z. Cai, J.E. Jones, S.F. McCormick, and T.F. Russell. Control-volume mixed finite element methods. *Comput. Geosci.*, 1:289–315, 1997.
[18] Z. Cai, J. Mandel, and S. McCormick. The finite volume element method for diffusion equations on general triangulations. *SIAM J. Numer. Anal.*, 28(2):392–402, 1991.
[19] Y. Caillabet, P. Fabrie, P. Landereau, B. Noetinger, and M. Quintard. Implementation of a finite-volume method for the determination of effective parameters in fissured porous media. *Numer. Meth. Part. D.E.*, 16:237–263, 2000.
[20] P. Castillo. A review of the local discontinuous Galerkin (LDG) method applied to elliptic problems. *Appl. Numer. Math.*, 56:1307–1313, 2006.
[21] Z. Chen. On the control volume finite element methods and their application to multiphase flow. *Networks and Heterogeneous Media*, 1(4):689–706, 2006.
[22] P.G. Ciarlet. *The finite element method for elliptic problems*. North-Holland, Amsterdam, 1980.
[23] Committee on Fracture Characterization and Fluid Flow, U.S. National Commitee for Rock Mechanics, Geotechnical Board, Board on Energy and Environmental Systems, Commission on Engineering and Technical Systems, and National Research Council. *Rock fractures and fluid flow : contemporary understanding and applications*. National Academy Press, Washington, D.C., 1996.
[24] A. Datta-Gupta and M.J. King. *Streamline simulation: Theory and practice*. SPE Text book, 2007.
[25] T. Davis. Comparison of CHOLMOD and the preconditioned conjugate gradient method. Available online: http://www.cise.ufl.edu/research/sparse/pcg_compare/, 2007.
[26] T.A. Davis. Umpfpack, unsymmetric multifrontal method. http://www.cise.ufl.edu/research/sparse/umfpack/, 2008.
[27] P. Dietrich, R. Helmig, M. Sauter, H. Hötzl, J. Köngeter, and G. Teutsch, editors. *Flow and transport in fractured porous media*. Springer, Berlin, 2005.
[28] M.G. Edwards and M. Pal. Positive-definite q-families of continuous sub-cell Darcy-flux CVD(MPFA) finite volume schemes and the mixed finte element method. *Int. J. Numer. Meth. Fluids*, 57:355–387, 2008.
[29] M.G. Edwards and C.F. Rogers. Finite volume discretization with imposed flux continuity for the general tensor pressure equation. *Computational Geosciences*, 2:259–290, 1998.
[30] G.T. Eigestad, I. Aavatsmark, and M. Espedal. Symmetry and M-matrix issues for the O-method on an unstructured grid. *Comput. Geosci.*, 6:381–404, 2002.
[31] G.T. Eigestad and R.A. Klausen. On the convergence of the multi-point flux approximation O-method: Numerical experiments for discontinuous permeability. *Numer. Meth. Part. D.E.*, 21(6):1079–1098, 2005.
[32] R.E. Ewing, T. Lin, and Y. Lin. On the accuracy of the finite volume element method based on piecewise linear polynomials. *SIAM J. Numer. Anal.*, 39(6):1865–1888, 2002.
[33] R. Eymard, T. Gallouët, and R. Herbin. Finite volume methods. In P.G. Ciarlet and J.L. Lions, editors, *Handbook of numerical analysis, vol. VII*. North-Holland, Amsterdam, 2000.
[34] A. Fuchs. *Optimierte Delaunay-Triangulierungen zur Vernetzung getrimmter NURBS-Körper*. PhD thesis, Stuttgart University, 1999.
[35] S. Gebauer, L. Neunhäuserer, R. Kornhuber, S. Ochs, R. Hinkelmann, and R. Helmig. Equidimensional modelling of flow and transport processes i fractured porous systems i. In Proc [56].
[36] G.H. Golub and C.F. Van Loan. *Matrix computations*. Johns Hopkins studies in the mathematical sciences ; 3. Johns Hopkins University Press, Baltimore, third edition, 1996.
[37] H. Hægland. *Streamline methods with application to flow in fractured media*. PhD thesis, Dept. of Mathematics, University of Bergen, Norway, 2009. In preparation.
[38] H. Hægland, A. Assteerawatt, R. Helmig, and H.K. Dahle. Simulation of flow and transport for a discrete fracture matrix system ii. effcient and accurate streamline approach. Submitted to *Water Resources Research*, 2008.

[39] N.J. Higham. *Accuracy and stability of numerical algorithms*. Society for Industrial and Applied Mathematics, Philadelphia, second edition, 2002.
[40] R. Holm, R. Kaufmann, B.-O. Heimsund, E. Øian, and M.S. Espedal. Meshing of domains with complex internal geometries. *Numerical Linear Algebra with Applications*, 13(9):717–731, 2006.
[41] H. Hoteit and A. Firoozabadi. Multicomponent fluid flow by discontinuous Galerkin and mixed methods in unfractured and fractured media. *Water Resour. Res.*, 41(W11412, doi:10.1029/2005WR004339), 2005.
[42] P.S. Huyakorn and G.F. Pinder. *Computational methods in subsurface flow*. Academic Press, New York, 1983.
[43] J. Hyman, M. Shashkov, and S. Steinberg. The numerical solution of diffusion problems in strongly heterogeneous non-isotropic materials. *J. Comput. Phys.*, 132:130–148, 1997.
[44] R. Juanes, J. Samper, and J. Molinero. A general and efficient formulation of fractures and boundary conditions in the finite element method. *Int. J. Numer. Methods Eng.*, 54:1751–1774, 2002.
[45] M. Karimi-Fard, L.J. Durlofsky, and K. Aziz. An efficient discrete fracture model applicable for general purpose reservoir simulators. *SPE J.*, pages 227–236, June 2004.
[46] J.-G. Kim and M.D. Deo. Finite element, discrete-fracture model for multiphase flow in porous media. *AIChE Journal*, 46(6):1120–1130, 2000.
[47] R.A. Klausen and R. Winther. Robust convergence of multi point flux approximation on rough grids. *Numer. Math.*, 104:317–337, 2006.
[48] R. Li, Z. Chen, and W. Wu. *Generalized difference methods for differential equations*. Marcel Dekker, New York, 2000.
[49] V. Martin, J. Jaffré, and J.E. Roberts. Modeling fractures and barriers as interfaces for flow in porous media. *SIAM J. Sci. Comput.*, 26(5):1667–1691, 2005.
[50] K.W. Morton and E. Süli. Finite volume methods and their analysis. *IMA Journal of Numerical Analysis*, 11:241–260, 1991.
[51] S.P. Neuman. Trends, prospects and challenges in quantifying flow and transport through fractured rocks. *Hydrogeology Journal*, 13:124–147, 2005.
[52] L. Neunhäuserer. *Diskretisierungsansätze zur Modellierung von Strömungs- und Transportprozessen in geklüftet-porösen Medien*. PhD thesis, University of Stuttgart, 2003.
[53] L. Neunhäuserer, S. Gebauer, S. Ochs, R. Hinkelmann, R. Kornhuber, and R. Helmig. Equidimensional modelling of flow and transport processes in fractured porous systems ii. In Proc [56].
[54] S.O. Ochs, R. Hinkelmann, N. Neunhäuserer, M. Suess, R. Helmig, S. Gebauer, and R. Kornhuber. Adaptive methods for the equidimensional modelling of flow and transport processes in fractured aquifers. In *5th International Conference on Hydro-Science & -Engineering, Warsaw, Poland*, 2002.
[55] C.F. Pinder, P.S. Huyakorn, and E.A. Sudicky. Simulation of flow and transport in fractured porous media. In J. Bear, C.-F. Tsang, and G. de Marsily, editors, *Flow and contaminant transport in fractured rock*, pages 395–435. Academic Press, San Diego, 1993.
[56] *Proceedings of the XIV International Conference on Computational Methods in Water Resources, vol. 1, 23-28 June, Delft, The Netherlands*, 2002.
[57] K. Pruess, J.S.Y. Wang, and Y.W. Tsang. On thermohydrologic conditions near high-level nuclear wastes emplaced in partially saturated fractured tuff. 1. simulation studies with explicit concideration of fracture effects. *Water Resour. Res.*, 26(6):1235–1248, 1990.
[58] V. Reichenberger, H. Jakobs, P. Bastian, and R. Helmig. A mixed-dimensional finite volume method for two-phase flow in fractured porous media. *Adv. Water Resour.*, 29(7):1020–1036, 2006.
[59] V. Reichenberger, H. Jakobs, P. Bastian, R. Helmig, and J. Niessner. Complex gas-water process in discrete fracture-matrix systems. Project report, 2006.

[60] M. Sahimi. *Flow and transport in porous media and fractured rock: From classical methods to modern approaches*. VCH, Weinheim, 1995.
[61] M. Shashkov and S. Steinberg. *Conservative finite-difference methods on general grids*. Symbolic and numeric computation series. CRC Press, Baca Raton, 1996.
[62] A. Silberhorn-Hemminger. *Modellierung von Kluftaquifersystemen: Geostatistische Analyse und deterministisch-stochastische Kluftgenerierung*. PhD thesis, University of Stuttgart, 2002.
[63] G.W. Stewart and J.-G. Sun. *Matrix pertubation theory*. Computer science and scientific computing. Academic press, Boston, 1990.
[64] G. Strang and G.J. Fix. *An analysis of the finite element method*. Prentice-Hall series in automatic computation. Prentice-Hall, Englewood Cliffs, N.J., 1973.
[65] *SPE Reservoir Simulation Symposium, Dallas, Texas, 8-11 June*, 1997.
[66] A. Teimoori, Z. Chen, S.S. Rahman, and T. Tran. Effective permeability calculation using boundary element method in naturally fractured reservoirs. *Petroleum Science And Technology*, 23:693–709, 2005.
[67] S. Verma and K. Aziz. A control-volume scheme for flexible grids in reservoir simulation, SPE 37999. In Symp [65].
[68] E.W. Weisstein. "Plane-Plane Intersection." from MathWorld–A wolfram web resource. http://mathworld.wolfram.com/Plane-PlaneIntersection.html.
[69] O.C. Zienkiewicz, R.L. Taylor, and J.Z. Zhu. *The finite element method : its basis and fundamentals*. Elsevier, Amsterdam, 6th edition, 2005.